Received: 17 August 2020 | Revised: 30 September 2020 | Accepted: 7 October 2020

DOI: 10.1002/xrs.3207

RESEARCH ARTICLE

X-RAY SPECTROMETRY WILEY

Vignetted photon fields, recharacterisation of V Kα, and reducing X-ray uncertainties by a factor of two

Jonathan W. Dean | **Christopher T. Chantler**

School of Physics, The University of Melbourne, Melbourne, Victoria, Australia

Correspondence
Christopher T. Chantler, School of Physics, The University of Melbourne, Melbourne, VIC, Australia.
Email: chantler@unimelb.edu.au

A vignetting profile form is incorporated with characteristic X-ray emission data from a Johann-mounted crystal diffractometer. We prove the validity of the specific form of the vignetting profile. A new characterisation of the Kα profile for vanadium is presented, which supports and is superior to the current benchmark. Using the profile form as a correction for systematic vignetting reduces energy uncertainties by up to a factor of two or more. The greater precision in measurement robustness allows current atomic theories and profiles to be tested with higher levels of accuracy.

1 | INTRODUCTION

X-ray diffraction is a widely used experimental technique in disciplines ranging from virology to particle physics. It is the most successful method for determining molecular structure in species ranging from small molecules like ferrocene[1] to large, complex protein structures such as *Blastochloris viridis*[2] and amyloid-β.[3] X-ray diffraction is also the only method to measure characteristic atomic energy eigenvalues for medium- to high-Z elements, which has widespread applications in chemistry,[4] astrophysics,[5] plasma physics,[6] nanopowders,[7] and agriculture.[8] Furthermore, accurate X-ray diffraction has the potential to give insights into new physics by testing fundamental constants in quantum electrodynamics.[9–12] Needless to say, significant improvements to determine photon energies in the X-ray regime will improve the quality of data and will further research in all these fields. Whilst conventional crystallography with wide angle detectors will usually not be aperture-limited except at the source, most areas of X-ray diffraction and X-ray spectroscopy are aperture-limited at source and detector so that the optics of spectral profiles are critical to insight. We have developed a method to significantly reduce a systematic uncertainty in X-ray spectroscopy and atomic physics. However, a similar reduction of errors can be made in all X-ray diffraction or spectroscopic measurements where propagating photon fields are truncated by a wedge or other aperture.

One immediate application of a vignetting profile fix is towards a recent study observing magnetic circular dichroism in Fe Kα emission.[13] From their Figure 2, in attempting to ensure the parallel nature of the photon field, vignetting may have occurred. Therefore, it should be tested for and if found, accounted for to strengthen the claims of the investigation.

X-ray diffraction involves a photon beam incident on a diffracting crystal, which has an output angle related to the photon energy. Therefore, measuring X-ray energies is akin to measuring angles. There are a few ways to achieve this measurement, each with advantages. One method uses a flat crystal with well-defined lattice spacing to use Bragg's law to establish the relationship between angle and energy.[14] Another method uses a Johann-type (curved) crystal spectrometer, with a strained lattice spacing, so must be calibrated to provide a reliable relationship between angle and energy.[15,16]

For both techniques, it is essential to ensure a highly parallel incoming photon beam. Two energy-degenerate but non-parallel photons will be detected at different angles, and therefore appear to be non-degenerate. Non-parallel photon fields lead to greater instrumental broadening, and uncertainties in collected data. Johann spectrometry has the crystal focussing all degenerate photons onto the Rowland circle. However, not all measurements for a given

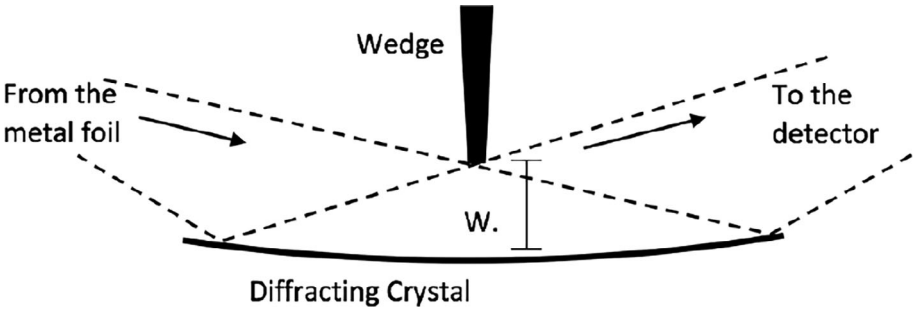

FIGURE 1 A side-on view of the crystal diffractometer and "Seeman" wedge setup. The smaller the gap *W*, the more parallel the out-coming photon beam

transition can be taken near the Rowland circle. To ensure a parallel photon field, an adjustable "Seeman" wedge limits the diffracting region of the crystal which in turn alters linearity and bandpass, as illustrated in Figure 1. There is a trade-off: Cut-off too much of the photon field, and it may be parallel, but it has also become vignetted—too narrow to fully represent the spectral profile. A vignetted beam is one which has a decreased photon intensity towards one edge of the beam due to optical collimation.

How do we minimise vignetting whilst achieve a more parallel incoming photon field? Previously, the answer has mostly been that no vignetting is permissible, as this will shift the final results for energy, which is the entire purpose of any energy measurement. Experimental Gaussian broadening can be accounted for by deconvolution so it is often recommended to have a broader bandpass to obtain a full but lower resolution spectrum. However, as we stray from the Rowland circle, the defocussing broadening becomes too great to obtain reliable profiles or structural insight.

This work explains that, through incorporating a reconstructed vignetted profile, accurate results are achieved—consistent with previous results even when a wedge has artificially shifted the recorded energy centroids. Furthermore, it has enabled some experiments to report uncertainties a factor of two lower which have enabled measurements to be taken with precisions not previously possible.[16]

2 | METHOD

The X-ray Optics and Synchrotron Science (XROSS) laboratory at The University of Melbourne uses a Johann diffractometer in conjunction with four gravity-referenced clinometers to take high accuracy measurements of energy from atomic emission spectra in the 4 to 8 keV range. A 20 keV electron gun beam is incident upon high purity (>99.99%) metal foils to create the fluorescence photons; these are diffracted by a curved germanium (220) crystal (with radius 1,121(10)mm and thickness

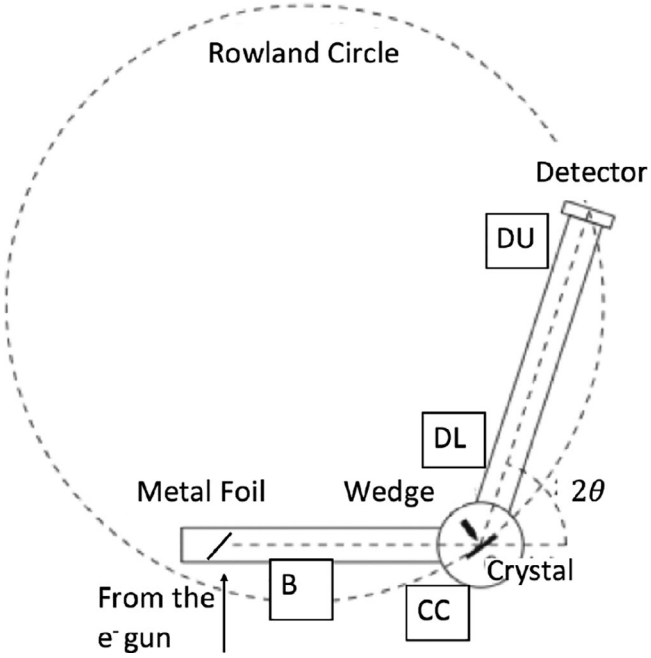

FIGURE 2 A schematic diagram of the experimental setup, not to scale. The approximate location of the four clinometers is given in square boxes. Relevant dimensions are given in Table 1. The detector is not always near the Rowland Circle as shown. Table 2 provides the distances between the two for various transitions used in this experiment

0.820(5)mm); through an adjustable "Seeman" wedge; to a multi-wire gas proportional counter with backgammon geometry; with angles monitored by four gravity-referenced clinometers placed at the base (B), the crystal housing (CC), the lower (DL) and upper (DU) portion of the detector arm. The detector arm length is 1,500(5)mm, source to crystal length is 330(5)mm, and the source width (FWHM) is 5(1)mm. The overall performance, count-rate, and linearity of the backgammon detector is discussed by Melia et al.[17] Figure 2 provides a schematic and Figure 3 gives a photograph of the diffractometer and source. Key geometric characteristics are given in Table 1.

The fluorescence incident on the crystal diffractometer must be close to parallel, or degenerate photons will

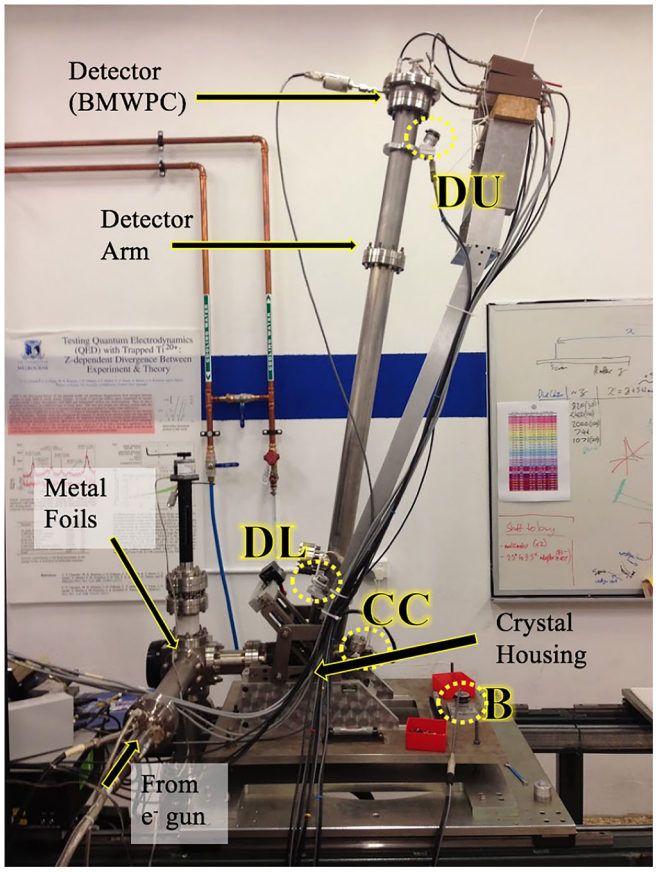

FIGURE 3 Photograph of the experimental setup

TABLE 1 The geometry of the experimental setup with estimated uncertainties

Parameter (symbol)	Value
Rowland circle radius (R_z)	1,121(10) mm
Detector arm length (ZF)	1,500(5) mm
Source to crystal length (BX_z)	330(5) mm
Source width (FWHM) (sw)	5(1) mm
Crystal thickness (T)	0.820(5) mm

Note: Numbers in parentheses are one standard error uncertainties of the quoted value referring to the last digits.

appear non-degenerate and lead to instrumental broadening or shifts. This is essential in studies with flat crystals. Mendenhall et al.[14] go to great lengths to ensure the parallel nature of their double crystal diffractometer and hence the photon field. With Johann spectrometry, the fluorescent photons are focussed onto the Rowland circle so that non-parallel fields are not so large an issue so long as the detector is near the Rowland circle. This is clear in our data without a wedge, Figures 5-8 show the Kα profiles of titanium, chromium, vanadium and manganese ($Z = 22 - 25$) and the distance from the Rowland circles to the detector is given in Table 2. The increase of instrumental broadening with distance from the Rowland circle is obvious. Only titanium—the profile where the detector is very close to the Rowland circle—has ideally resolved Kα_1 and Kα_2 peaks for an "open" wedge.

Since there is no well-defined crystal lattice spacing for curved crystals, the detector arm angle must be calibrated. This is typically done using transitions that have low uncertainties in the current literature to build an angular dispersion function that will relate angle and energy. This involves moving the detector arm to observe a range of different transitions. Therefore, the detector will not be in the region close to the Rowland circle for the entire experiment, making the wedge an essential piece of apparatus.

3 | DISPERSION FUNCTION

For flat crystals, the Bragg condition is the particularly simple relationship between photon energy and diffraction angle. However, for curved crystals, the relationship is more complex and must be predicted and tested by dynamical diffraction theory.

There are three clinometers: the crystal clinometer (CC), detector upper (DU), and detector lower (DL), each referenced to the base clinometer (B). The raw outputs are voltages. These clinometers are calibrated to great angular precision to obtain a precise dispersion function and therefore energy, using well-defined literature values for other transitions in a similar region to the target transition. We show the transitions used by a recent publication[16] with the aim of characterising Sc Kα in Table 3.

For accurate or even good calibration, peak energies of K$\alpha_{1,2}$ are insufficient. X-ray emission from electron bombardment undergoes many processes with contributions in the spectra from many energy eigenstates (from relativistic multi-configuration DHF computations) ranging from the tens to the tens-of-thousands depending on the transition. Whilst this theory is undergoing great advances at this time (e.g., GRASP2K),[5,19–22] it is known that convergence is difficult as is comparing a partially resolved spectrum with thousands of eigenvalues and amplitudes. The most detailed current characterisations of experimental spectra are given in the International Tables for Crystallography, Vol. C[18] and, for example, ref. [16] as well as papers sourced in those references. Hence, it is common in recent literature for 3d transition metals to be described with six Voigts for Kα and five for Kβ. Indeed, according to the goodness-of-fit measure χ^2_r this often yields values near unity and ergo matches the information content of the experimental spectra. Hence, we here use the full characterisation (six Voigts for Kα and five for Kβ) required as discussed therein. The Kα and Kβ transitions are modelled with a

TABLE 2 *D*, the absolute distance between the detector and the Rowland circle

Transition	Sc Kα	Ti Kα	V Kα	Cr Kα	Mn Kα
D (cm)	16.82(1)	3.69(1)	7.09(1)	16.08(1)	23.44(1)

Note: Comparing the distances given here to Figures 5-8, the relationship between the instrumental broadening and the distance to the Rowland circle is clear. Numbers in parentheses are one standard error uncertainties of the quoted value in the last digits.

TABLE 3 Reconstructed peak energy values (zero Gaussian broadening) for the calibration K$\alpha_{1,2}$ and Kβ lines

Element	Kα_1 (eV)	Kα_2 (eV)	Kβ (eV)
Ti ($Z = 22$)	4,510.901(10)	4,504.911(7)	4,931.996(22)
V ($Z = 23$)	4,952.224(18)	4,944.652(48)	5,427.320(71)
Cr ($Z = 24$)	5,415.536(3)	5,405.512(5)	5,946.823(11)
Mn ($Z = 25$)	5,898.858(5)	5,887.740(5)	6,490.585(14)

Note: The diagram K$\alpha_{1,2}$ and Kβ lines are quite insufficient to give an accurate calibration. Rather the full (six Voigt for Kα; five Voigt for Kβ) characterisation is used. Numbers in parentheses are one standard error uncertainties in the last digits. Values are taken from the International Tables for Crystallography, Vol. C.[18]

constant background value, B, and n-Voigt profiles, with parameters of Lorentzian width, W; centroid position, C; amplitude, A; and each with a common Gaussian width, σ:

$$I(E;B,\sigma,A_i,C_i,W_i) = B + \sum_{i=0}^{n} V(E;A_i,C_i,W_i,\sigma) \qquad (1)$$

where the Voigt profile is the convolution between a Gaussian and a Lorentzian and $n = 6$ for Kα, $n = 5$ for Kβ.

Whilst Bragg's law for a flat crystal is insufficient for curved crystals, there are theoretical models for obtaining the diffraction profile for curved crystals. One method is the *Moscurve* theory derived by Chantler and implemented in the *Mosplate* software.[23,24] This takes the geometric parameters in Table 1 and the crystal plane of diffraction (Ge 220 in this experiment) to derive a diffraction profile incident on the detector face as a function of photon energy, E, and detector arm angle, θ:

$$x = X_{\text{mosplate}}(E,\theta) \qquad (2)$$

Also provided by the Mosplate code are the inverse functions:

$$\theta = \Theta_{\text{mosplate}}(E,x);\ E = E_{\text{mosplate}}(\theta,x) \qquad (3)$$

With these equations, the energies in Table 3 and the detector x-values calibrate the clinometers. Calibration defines the dispersion function which takes the raw voltage output from the clinometers and returns an angle for the detector arm, $\theta = \Theta_{\text{dispersion}}(V)$. Once the dispersion function is defined, the target transition energy is measured through Equation 3, $E = E_{\text{mosplate}}(\Theta_{\text{dispersion}}, x)$. The specific form of the dispersion function is dependent on the number of calibration lines and the particular apparatus being used. For ref. [16], the following is used:

$$\Theta_{\text{disp}}(VP_i) = \arcsin\left(\frac{V-P_2}{P_0}\right) - P_1 + \sum_{i=0}^{n} P_{(i+3)}(V-P_2)^i \qquad (4)$$

where the parameters P_i are found through least-squares fitting via the Levenburg-Marquardt algorithm. There is one dispersion function for each clinometer. An example for the CC dispersion function is given in Figure 4. Superficially and locally, it looks very much like a simple linear and monotonic function. Experimentally, the detail and accuracy arises from inspection of the scatter of independent measurements, the variation with the wedge aperture, and the residuals of the fit.

As well as a detector arm dispersion function matching voltage and angle to a reference point on the detector, there is a detector face dispersion function defining variation of energy and angle with the position x across the detector face. A meander wire proportional counter has voltage as raw output. There are inevitably certain systematics to shift the apparent position of an X-ray event, including electromagnetic edge effects and detector wire non-uniformity.[17]

Several calibration transitions are used to reduce the fitting uncertainty to construct the dispersion function by using more data and more repetitions. Figures 5-8 demonstrates that the further away from the Rowland circle the detector face is, the greater the instrumental broadening becomes. In some instances, the data are too broad and unusable.

Introduction of the Seeman wedge to limit the diffracting area of the crystal and therefore increase the parallelism of the incoming photon field enables data to be used that otherwise would have been unusable. However, when narrowing the wedge aperture, there is the possibility of vignetting the data. This introduces a new

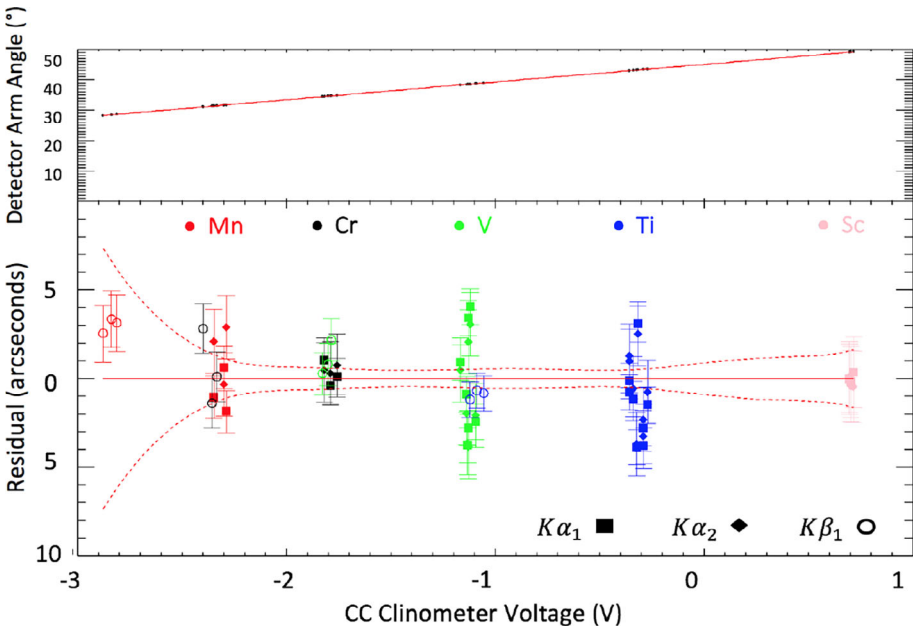

FIGURE 4 The CC dispersion function with the residuals shown for each calibration reconstructed peak energy value. The red dotted line shows the 1σ uncertainty of the final dispersion function which incorporates all three clinometers. The error bars for each reconstructed peak is shown in the residual plot. The full *n*-Voigt characterisation is used to define a dispersion function, rather than the diagram reconstructed peak energies. We show the diagram lines as calibration points for ease of viewing

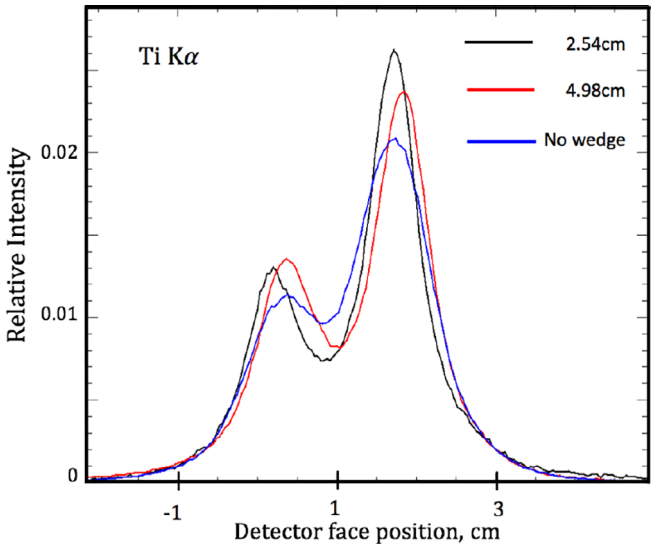

FIGURE 5 Ti Kα profile, $D = 3.69(1)$cm. The wedge position is indicated in the legend. Each profile is normalised to have the same unity *integrated* intensity

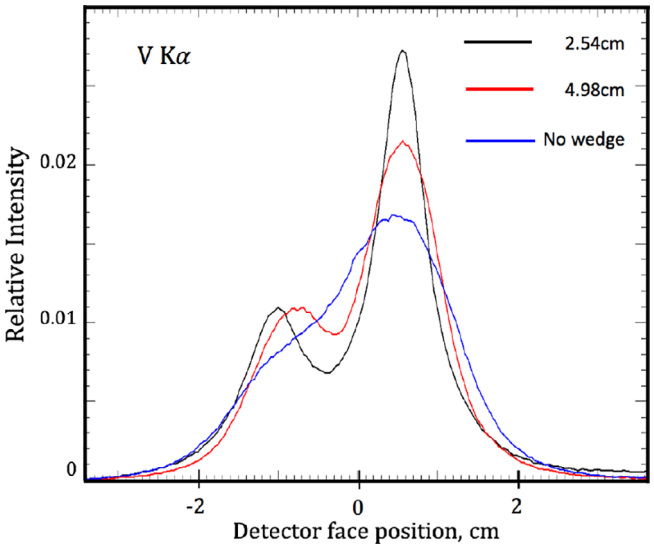

FIGURE 6 V Kα profile, $D = 7.09(1)$cm

uncertainty to the system. The centre of mass of the resulting profile can shift to a higher or a lower energy.

We solve this issue with the reconstruction of a vignetting profile. This enables a wedge to be used to collect usable data, whilst not introducing a vignetting systematic error to the recorded centre of mass.

4 | VIGNETTING

Vignetting is any decrease in intensity towards the edges of a detector due to collimation by an aperture or effective loss of a uniform convolution. It can occur in any optical measurement from visible spectrum astrophysics[25] and infrared optics[26] to X-ray optics,[27] and is a critical consideration in the camera manufacturing industry and visible optics.[28]

Experimentalists would rather design their experiments with no vignetting. However, this is not always possible, and in curved crystal experiments can significantly reduce the number of profiles collected and hence the characterisation of energy or profile as the detector moves away from the Rowland circle (Figures 5-8).

Figures 5-8 are plotted such that each profile has unity *integrated* intensity. This helps compare the broadening of the profiles as the wedge size increases. The

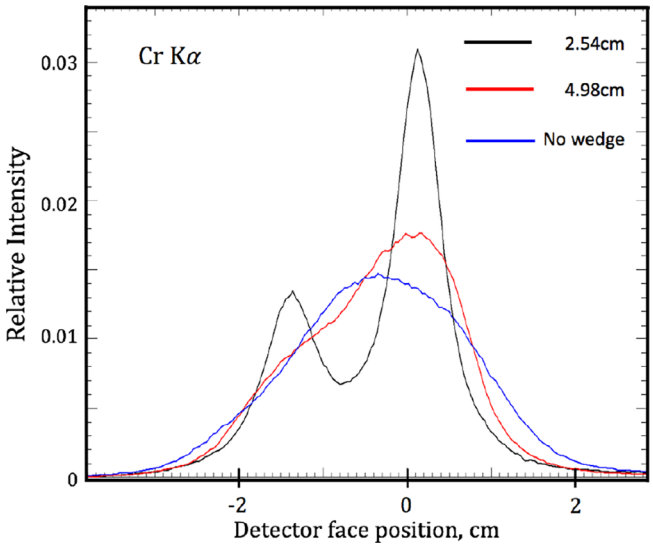

FIGURE 7 Cr Kα profile, $D = 16.08(1)$cm

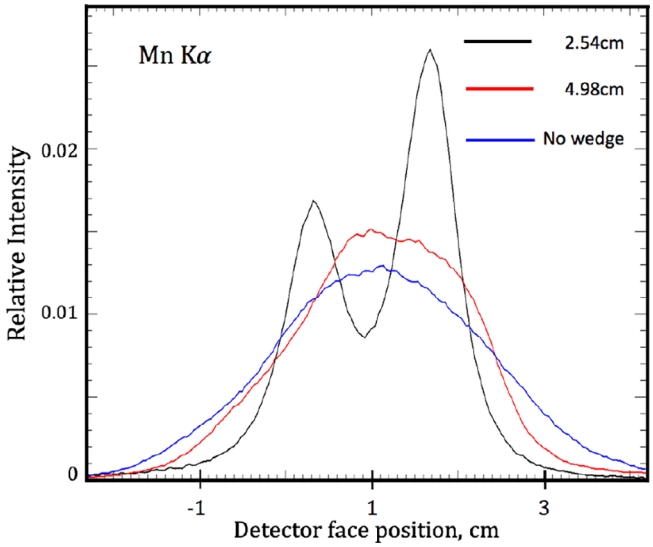

FIGURE 8 Mn Kα profile, $D = 23.44(1)$cm

tighter the wedge constraint, the lower the flux of photons through per unit time, and therefore the lower the absolute intensity. We increase the counting time accordingly for the smaller wedge sizes. Clearly, as the detector moves further from the Rowland circle to match the Bragg condition, a wedge is needed to ensure the data is not too broad. However, the wedge is a source of systematic uncertainty through vignetting the data. Consider Figures 9 and 10 showing two spectra, taken from the right-hand side (RHS, high energy) and left-hand side (LHS, low energy) of the detector face, respectively. Fitted to our data are the current best literature characterisations for those spectra[18] with free parameters for: Gaussian broadening, background counts, and a constant amplitude scaling factor. Both spectra have been

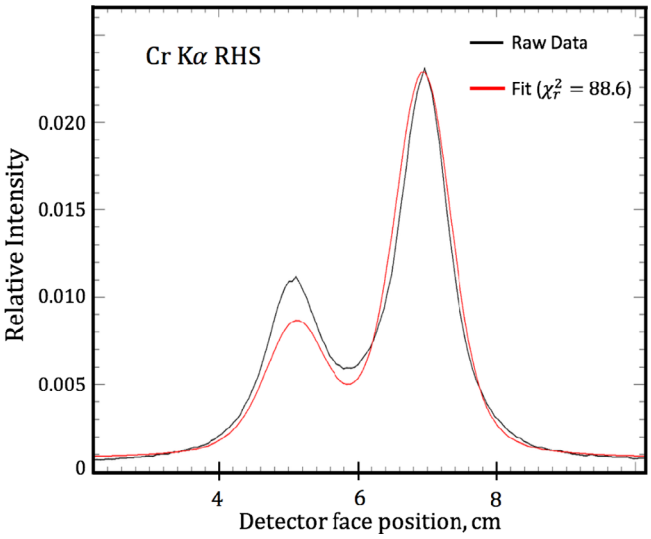

FIGURE 9 A profile taken on the right-hand side of the detector face with the narrowest wedge, 2.54 cm. The model does not fit the data. The photons incident towards the right side of the detector face are being vignetted by the wedge and therefore prevented from reaching the detector. This explains the significantly greater value for the Kα_2 peak for our data compared to the model and theoretical predictions

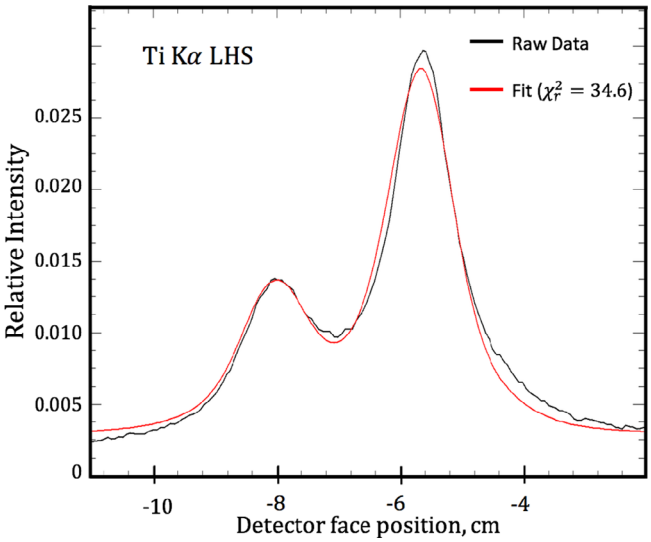

FIGURE 10 Similar to Figure 9, but with the profile on the left-hand side of the detector face. The vignetting of the photons towards the left side of the detector causes the Kα_1 peak to have a greater amplitude for the data compared to the fit

taken with the smallest wedge, highlighting the effect of vignetting. The effect is visible when comparing our data to the current theoretical model and observing a significantly reduced peak for Kα_2 in the RHS fit (Figure 9) and a reduced Kα_1 peak for the LHS fit (Figure 10). Previously, this data would not have been used in the dispersion function, as the fitting χ_r^2 are too large to be a

reliable calibration line (i.e., the model function does not fit the data). A reduction in one of the peaks of the fit for a profile also indicates a reduction in the data for *the other peak*. That is, the RHS profile has reduced data in the Kα_1 peak and therefore it is vignetted on the RHS.

So in Johann crystal diffractometer spectrometry, omitting a wedge gives extremely broad spectra when the detector is far from the Rowland circle (Figures 5-8), and using a wedge incorporates a systematic which makes vignetted profiles unreliable. This has been a consistent trade-off in many diffraction experiments. However, the reconstruction of a vignetting profile solves this dilemma.

Vignetting is largely dependent on the wedge separation and the location of the centroid of the profile on the detector face. The more narrow the wedge, and the further to the edges of the detector the profiles are, the more likely it is that a profile will be vignetted. We determine when vignetting has occurred by measuring the ratio between the model and observed Kα_1 and Kα_2 peak amplitudes, A. When this ratio is not near unity, vignetting has occurred. For example, if $A(\mathrm{K}\alpha_{1,\mathrm{model}})/A(\mathrm{K}\alpha_{1,\mathrm{data}}) > 1.05$ or $A(\mathrm{K}\alpha_{2,\mathrm{model}})/A(\mathrm{K}\alpha_{2,\mathrm{data}}) < 0.95$ then we can say that RHS (high energy) vignetting has occurred.

The vignetting suppression at a point on the profile will take a value between zero (unimpeded) and one (fully occluded), and hence is a multiplier indicating what fraction of photons have been allowed to reach the given x-coordinate of the detector face due to the wedge.

There is no consensus in the literature as to the particular form of a vignetting profile, however there is good evidence for a linear ramp function.[28,29] A recent investigation has confirmed that the vignetting profile is linear to first order, with higher order effects leading to oscillations about the linear slope.[30] These oscillations become higher in frequency and lower in amplitude with increasing photon energy. Therefore, in the X-ray regime the linear functional is a very good approximation.

We define two vignetting ramp functions, $\tau_{\mathrm{LHS}}(x)$ and $\tau_{\mathrm{LHS}}(x)$, where $\tau \in [0, 1]$ and can be thought of as the fraction of photons cut-off from the detector face with $\tau = 0$ for photons completely prevented from accessing a certain part of the detector, $\tau = 1$ for no vignetting:

$$\tau_{\mathrm{RHS}}(x) = \begin{cases} 1 & x < V_1 \\ 1 - \dfrac{1-V_h}{V_2-V_1}(x-V_1) & V_1 \leq x \geq V_2 \\ V_h & x > V_2 \end{cases} \quad (5)$$

$$\tau_{LHS}(x) = \begin{cases} V_h & x < V_1 \\ V_h + \dfrac{1-V_h}{V_2-V_1}(x-V_1) & V_1 \leq x \geq V_2 \\ 1 & x > V_2 \end{cases} \quad (6)$$

where V_h is the maximum amount of vignetting ($V_h \in [0, 1]$) and V_1, V_2 are the start and end x-axis (energy) position for the vignetting ramp. Therefore, the full vignetting model is the product of the vignetting slope and original model of six Voigts (1):

$$I'(E) = B + \left(\sum_{i=0}^{n} V(E; A_i, C_i, W_i, \sigma)\right) \tau_{\mathrm{RHS/LHS}}(E) \quad (7)$$

where we can translate between detector x-coordinates and energy, E, using the Mosplate theoretical predictions, following 2 and 3.

We test the effectiveness of a linear vignetting correction applied to the profiles from Figures 9 to 10 (Figures 11 and 12) with the x-axis scaled from the detector x-values to the energy-axis using Equation 2. The significant decrease in χ_r^2, gives strong confidence in the validity of the model functional and in using the data as calibration lines.

The only new free parameters in the fitting procedure are the vignetting constants V_h, V_1, V_2. Each Voigt is still modelled using the literature values. It is remarkable how consistent our results are with those of previous experiments and with our other data not affected by vignetting. This level of consistency proves the physical significance of the functional.

Further evidence that this is a physically real phenomena, and the linear slope is the correct model is given when

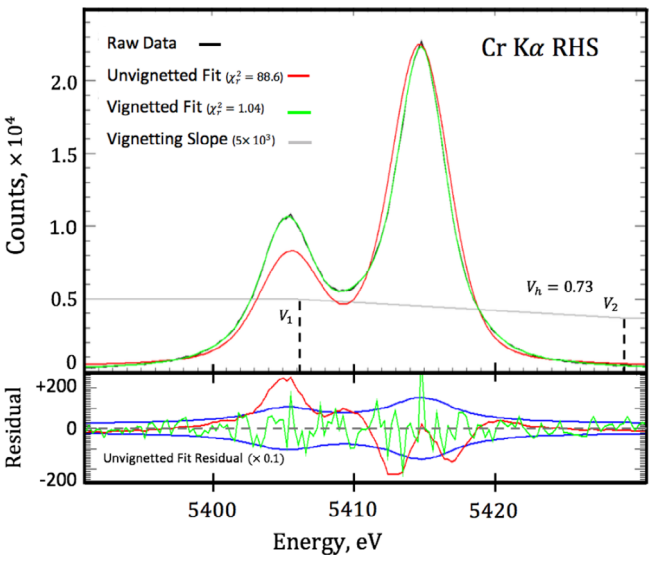

FIGURE 11 The data (black) and unvignetted fit (red) from Figure 9 with the modelled vignetting fit (green, Equation 7) and vignetting slope (grey, Equation 5). The χ_r^2 improvement is highly significant and strong evidence of both vignetting and of the model function. The residual of the unvignetted fit has been scaled by a factor of 0.1 for ease of viewing, otherwise it would dominate the residual plot and the vignetted residual would not be visible

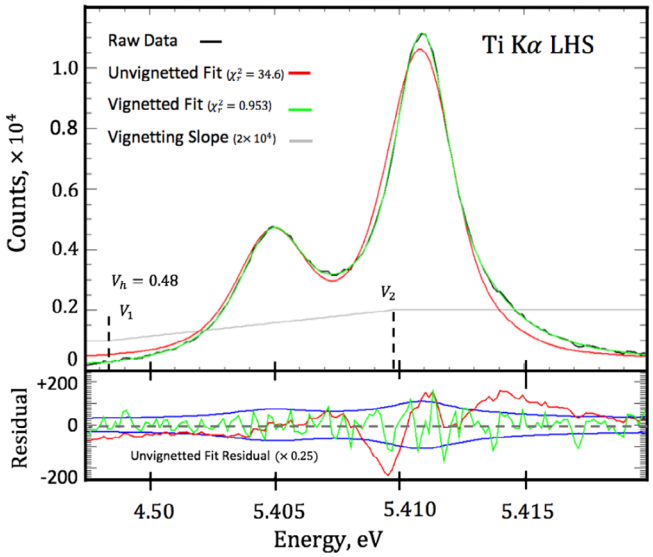

FIGURE 12 The data (black) and unvignetted fit (red) from Figure 10 with the modelled vignetting fit (green, Equation 7) and vignetting slope (grey, Equation 6). Similarly, the χ_r^2 is improved dramatically and the unvignetted residuals are plotted scaled by a factor of 0.25

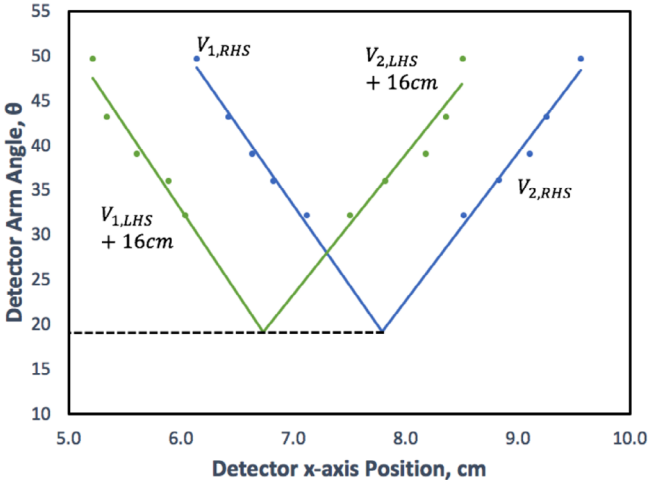

FIGURE 13 Plots of the starting (V_1) and ending (V_2) points of the vignetting slopes for the narrowest wedge (2.54 cm) for both the RHS and LHS profiles. The LHS profile parameters have been shifted to be in the same plot. There is a remarkable consistency between the RHS and LHS parameters. Most notably, where the lined of best fit overlap is at almost the same point for each, 19.45˚ for RHS and 19.51˚ for LHS

considering how the values for V_1 and V_2 change as the detector arm angle changes. As the detector arm angle decreases, so should the amount of vignetting. This is due to simple geometry of the wedge and visible in Figure 1. For a fixed wedge, the region of the crystal cut-off from the source, or propagating towards the detector, decreases with a decreased detector arm angle. Each transition has a different Bragg angle, and we can test where the start and end points of the vignetting slope are for both the RHS profiles and the LHS profiles. The results of this are given in Figure 13.

By extending the lines of best fit for each of the pairs of slopes (LHS/RHS pairs), it matches the hypothesis that as the detector arm angle decreases, so too does the amount of vignetting. In fact, at about 20˚ it appears there would be no vignetting at this wedge spacing.

Overall, the effect of vignetting in the dispersion function, and therefore the precision of angle measurements, is seen when comparing the dispersion function in Figure 4 to the dispersion function where no vignetting profiles are accounted for in Figure 14. This linear ramp functional for vignetting accurately models the physical phenomenon with strong robustness.

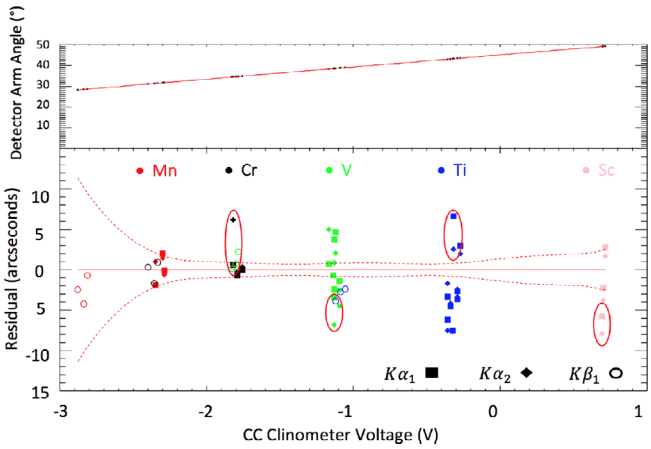

FIGURE 14 The CC clinometer dispersion function when no vignetting profile is accounted for. A red circle is drawn to highlight pairs of points that are very discrepant, due to particular profiles having significant vignetting distortion. The uncertainty in the function is a factor of two larger than before. The individual error bars for each point are not included for ease of viewing

5 | REDUCTION OF UNCERTAINTY BY A FACTOR OF TWO

One result of implementing a stable and robust vignetting function has already been discussed, this is the work by Dean et al. measuring the characteristic X-ray radiation of Sc to 2 ppm.[16] Section 4.1 from Dean et al. they claim their vignetting function attributes a factor of three lower χ_r^2 in the fitting of the spectra. Furthermore, in Table 3, Dean et al. show the value for their experiment if they could only use non-vignetted calibration lines, which has an uncertainty twice that of what they can achieve through the fitting of a vignetting profile. Dean et al. were able to determine which of their profiles had been vignetted, and therefore either remove them entirely or employ a vignetting profile. If the vignetted

profiles had been included without understanding that they were misleading, they would have arrived at a dispersion function in Figure 14. Oversight like this can lead to systematic errors unaccounted for in the error analysis and provides results with greater than deserved confidence.

6 | RECHARACTERISATION OF V Kα

The most recent characterisation of vanadium Kα is ref. [31]. They report a Gaussian width of 1.99 eV which is significantly higher than other 3d transition metals. Therefore, we have performed a recharacterisation of this profile and have been able to report a significantly lower Gaussian broadening. Based on this lower experimental broadening, noting that our results are consistent with ref. [31], and noting that our parameter uncertainties are smaller than ref. [31], this characterisation should replace the standard. We present our characterisation, along with that from ref. [31] and the difference between the two in Table 4.

The greatest concern relating to ref. [31] is that their result of Vanadium Kα has a Gaussian broadening of 1.99(12) eV where all the other transitions measured in the same study have broadening less than 0.7 eV. Whilst this in itself is no serious cause for alarm, it suggests remeasurement to determine whether a fit with less instrumental broadening will result in a similar characterisation.

When fitting the parameters for the six Voigt characterisation, the Levenberg–Marquardt least-squares algorithm is used. The initial guess is taken as the characterisation from ref. [31]. To best compare with ref. [31], each of the Voigt's three independent parameters (Lorentzian width, centroid position, and Relative amplitude) are tied to move by a constant amount, rather than individually. Further, we allow a small shift of the value of each parameter's estimated 1 standard deviation error bar following ref. [31]. It is a good sign that only 2 of the 18 Voigt parameters were actually constrained by this. In

TABLE 4 The values for the characterisation of V Kα using six Voigt profiles

Peak i	Centroid, C_i	Width, W_i	Relative amplitude, A_i
Chantler et al.[31]			
α_{11}	4,952.237(12)	1.45(2)	0.546(10)
α_{12}	4,950.656(184)	2.00(3)	0.114(1)
α_{13}	4,948.266(261)	1.81(70)	0.032(7)
α_{15}	4,955.269(141)	1.76(30)	0.020(2)
α_{21}	4,944.672(21)	2.94(4)	0.274(2)
α_{22}	4,943.014(303)	3.09(26)	0.013(1)
G width	1.99(12) eV		
This work			
α_{11}	4,952.220(9)	1.52(2)	0.545(8)
α_{12}	4,950.604(130)	2.01(3)	0.115(1)
α_{13}	4,948.321(181)	2.13(68)	0.028(5)
α_{15}	4,955.194(94)	1.72(22)	0.022(2)
α_{21}	4,944.668(14)	2.98(3)	0.275(2)
α_{22}	4,942.978(103)	3.02(20)	0.014(3)
G width	0.89(10) eV		
Difference			
α_{11}	0.017	−0.07	0.001
α_{12}	0.052	−0.01	−0.001
α_{13}	−0.055	−0.32	0.004
α_{15}	0.075	0.04	−0.002
α_{21}	0.004	−0.04	−0.001
α_{22}	0.036	0.07	−0.001

Note: Numbers in parentheses are one standard error uncertainties of the quoted value referring to the last digits. The difference is taken as ref. [31] subtract this work.

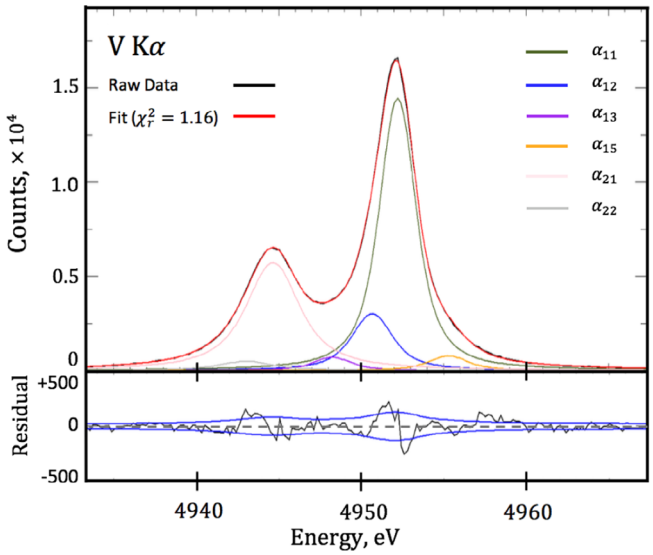

FIGURE 15 The V Kα profile, with six Voigt profiles. The background has been subtracted away from the data in plotting

Table 4, we present these final values, and the difference between our value and ref. [31]. The profile corresponding to our results in Table 4 are given in Figure 15. Overall, the recharacterisation supports,[31] as the best fit is found within error of theirs. However, this new characterisation appears superior due to most (12) parameter uncertainties decreasing, five staying constant, and only one increasing.

7 | DISCUSSION AND CONCLUSION

The use of a dispersion function to calibrate gravity-referenced clinometers to obtain high accuracy measurements for angle, and therefore energy, with Johann-type diffractometers has been well established as a state-of-the-art method. This work has showed that there are further improvements that can be made to data of this type. We expect that vignetting has been undetected, and uncorrected, in numerous past investigations. This may cause shifts in energy centroids, causing conflict between empirical evidence and theoretical calculations.

At the very least, by acknowledging and allowing for vignetting and correcting for it, Gaussian (instrumental) broadening may be significantly reduced by implementing a "Seeman" wedge. The vignetting profile is not limited to the X-ray regime of the electromagnetic spectrum. The scale of such a spectrum will of course change with energy, however, the specific shape should remain linear to first order.

We provide a new characterisation for the V Kα profile that fits well with the previous best characterisation, with Gaussian broadening reduced by a factor of two. This novel characterisation should replace the earlier reference characterisation.[31] Most (12) parameter uncertainties decrease, five stay constant, and only one parameter uncertainty increases. This should be uncontroversial: all but 2 of the 18 Voigt parameters are within the prior 1 standard uncertainty error.[31]

ORCID

Christopher T. Chantler https://orcid.org/0000-0001-6608-0048

REFERENCES

[1] C. T. Chantler, N. A. Rae, M. T. Islam, S. P. Best, J. Yeo, L. F. Smale, J. Hester, N. Mohammadi, F. Wang, *J. Sync. Rad.* **2012**, *19*(2), 145–158.
[2] L. Johansson, D. Arnlund, G. Katona, A. B. T. A. White, D. P. DePonte, R. L. Shoeman, C. Wickstrand, A. Sharma, G. J. Williams, A. Aquila, *Nature Comms.* **2013**, *2911*, 4.
[3] V. A. Streltsov, R. S. K. Ekanayake, S. C. Drew, C. T. Chantler, S. P. Best, *Inorg. Chem.* **2018**, *57*(18), 11422–11435.
[4] V. I. Vovna, E. P. Domashevskaya, A. V. Okotrub, *J. Struct. Chem.* **2017**, *58*(6), 1057–1060.
[5] C. T. Chantler, J. A. Lowe, I. P. Grant, *Notices Royal Astro. Soc.* **2014**, *440*(4), 3439–3443.
[6] S. B. Hansen, A. Y. Faenov, T. A. Pikuz, K. B. Fournier, R. Shepherd, H. Chen, K. Widmann, S. C. Wilks, Y. Ping, H. K. Chung, A. Niles, J. R. Hunter, G. Dyer, T. Ditmire, *Phys. Rev. E* **2005**, *72*(3), 036408.
[7] L. Armelao, G. Bottaro, M. Pascolini, M. Sessolo, E. Tondello, M. Bettinelli, A. Speghini, *J. Phys. Chem. C* **2008**, *112*(11), 4049–4054.
[8] L. Perring, A. Cotard, S. Al Sayadi, S. Berrut, *X-ray Spec.* **2019**, *48*(5), 395–400.
[9] P. Beiersdorfer, N. Hell, D. Panchenko, G. V. Brown, E. Träbert, R. L. Kelley, C. A. Kilbourne, F. Porter, *X-Ray Spec.* **2020**, *49*(1), 21–24.
[10] C. T. Chantler, M. N. Kinnane, J. D. Gillaspy, L. T. Hudson, A. T. Payne, L. F. Smale, A. Henins, J. M. Pomeroy, J. N. Tan, J. A. Kimpton, E. Takacs, K. Makonyi, *Phys. Rev. Lett.* **2012**, *109*(15), 153001.
[11] J. D. Gillaspy, C. T. Chantler, D. Paterson, L. T. Hudson, F. G. Serpa, E. Takacs, *J. Phys. B* **2010**, *43*(7), 074021.
[12] A. T. Payne, C. T. Chantler, M. N. Kinnane, J. D. Gillaspy, L. T. Hudson, L. F. Smale, A. Henins, J. A. Kimpton, E. Takacs, *J. Phys. B* **2014**, *47*(18), 185001.
[13] T. Inami, *Phys. Rev. Lett.* **2017**, *119*(13), 1–5.
[14] M. H. Mendenhall, A. Henins, L. T. Hudson, C. I. Szabo, D. Windover, J. P. Cline, *J. Phys. B* **2017**, *50*(11), 115004.
[15] F. Zeeshan, J. Hoszowska, J.-C. Dousse, D. Sokaras, T.-C. Weng, R. Alonso-Mori, M. Kavi, M. Guerra, J. M. Sampaio, F. Parente, P. Indelicato, J. P. Marques, J. P. Santos, *X-Ray Spec.* **2019**, *48*(5), 351–359.
[16] J. W. Dean, H. A. Melia, C. T. Chantler, L. F. Smale, *J. Phys. B* **2019**, *52*(16), 165002.

[17] H. A. Melia, J. W. Dean, C. T. Chantler, L. F. Smale, A. J. Illig, *X-Ray Spec.* **2019**, *48*(3), 218–231.
[18] C. T. Chantler, L. F. Smale, L. T. Hudson, X-ray energies. in *International Tables for Crystallography, Vol. C, Ch. 4.2* (Ed: T. R. Welberry), Kluwer Academic Publishers, Dordrecht **2020**, p. 2.
[19] P. Jönsson, G. Gaigalas, J. Bieroń, C. Froese-Fischer, I. P. Grant, *Comp. Phys. Commun* **2013**, *184*(9), 2197–2203.
[20] C. T. Chantler, T. V. B. Nguyen, J. A. Lowe, I. P. Grant, *Phys. Rev. A* **2014**, *90*, 062504.
[21] T. L. H. Pham, T. V. B. Nguyen, J. A. Lowe, I. P. Grant, C. T. Chantler, *J. Phys. B* **2016**, *49*, 035601.
[22] T. V. B. Nguyen, J. A. Lowe, T. L. H. Pham, I. P. Grant, C. T. Chantler, *Self-energy corrections in GRASP2K: Update and benchmark, with code for QED and gauge investigations*. The modified grasp2k package, dubbed version 1.15 **2015**. www.ph.unimelb.edu.au/chantler/opticshome/softwarepackagedownloads.html#GRASP2KRCISE.
[23] C. T. Chantler, *J. App. Cryst.* **1991**, *25*(6), 674–693.
[24] C. T. Chantler, *J. App. Cryst.* **1991**, *25*(6), 694–713.
[25] Y. Xue, H.-M. Shi, *Chinese J. Astro. Astrophys.* **2008**, *8*(5), 580–590.
[26] M. Zhu, Study on vignetting simulation method of infrared optical system, in *2009 International Conference on Environmental Science and Information Application* Technology, **2009**, *3*, 675–678.
[27] J. Shin, T. Sakurai, *Solar Phys.* **2016**, *291*(2), 705–725.
[28] A. Kordecki, H. Palus, A. Bal, Fast vignetting reduction method for digital still camera, in *2015 20th International Conference on Methods and Models in Automation and Robotics (MMAR)*, **2015**, 1145–1150.
[29] T. Ramsay, *Imaging Sci. J.* **2017**, *65*, 299–307.
[30] M. D. Davidović, M. D. Davidović, A. S. Sanz, M. Božić, D. Vasiljević, *J. Russian Laser Res.* **2018**, *39*(5), 438–447.
[31] C. T. Chantler, M. N. Kinnane, C.-H. Su, J. A. Kimpton, *Phys. Rev. A* **2006**, *73*, 012508.

How to cite this article: Dean JW, Chantler CT. Vignetted photon fields, recharacterisation of V Kα, and reducing X-ray uncertainties by a factor of two. *X-Ray Spectrom*. 2020;1–11. https://doi.org/10.1002/xrs.3207